Measuring shape and size of micrometric particles from the analysis of the forward scattered field

S. Villa, T. Sanvito, B. Paroli, A. Pullia, B. Delmonte, and M. A. C. Potenza'

Citation: Journal of Applied Physics **119**, 224901 (2016); doi: 10.1063/1.4953332
View online: http://dx.doi.org/10.1063/1.4953332
View Table of Contents: http://aip.scitation.org/toc/jap/119/22
Published by the American Institute of Physics

Measuring shape and size of micrometric particles from the analysis of the forward scattered field

S. Villa,[1] T. Sanvito,[2,3] B. Paroli,[1] A. Pullia,[1] B. Delmonte,[2] and M. A. C. Potenza[1,a)]
[1]*Department of Physics and CIMAINA, University of Milan, via Celoria 16, I-20133 Milan, Italy*
[2]*DISAT Department of Earth and Environmental Sciences, University Milano-Bicocca, Milan, Italy*
[3]*EOS s.r.l., viale Ortles 22/4, 20139 Milan, Italy*

(Received 1 February 2016; accepted 13 May 2016; published online 9 June 2016)

Characterizing nano- and micro-particles in fluids still proves to be a significant challenge for both science and industry. Here, we show how to determine shape and size distributions of polydisperse water suspensions of micron-sized particles by the analysis of the field scattered in the forward direction by single particles illuminated by a laser beam. We exploit the novel Single Particle Extinction and Scattering method in connection with shear conditions which give preferred orientations to the particles passing through the scattering volume. Water suspensions of calibrated non-spherical particles, polydisperse standard monophasic mineral samples of quartz and kaolinite, and a mixture of quartz and illite are studied in detail. Application and limitation of the method are discussed. *Published by AIP Publishing*. [http://dx.doi.org/10.1063/1.4953332]

I. INTRODUCTION

Characterizing micro- and nano-sized particles is a need of increasing importance for a number of scientific and technological applications. Particle size distribution (PSD), shapes, composition, and internal structure are of great importance to the understanding and foreseeing of the behavior of the particles. Interactions between particles, as well as between particles and surrounding media are mainly given by size, shape, composition, and surface properties, are important actors in this realm of increasing importance worldwide.[1] The need of continuous, non-invasive, in-line monitoring of powder suspensions in fluids is increasing, in connection with the rapid development of materials and devices through the bottom-up approach[2–8] as well as the need of characterizing small particles in the traditional top-down processes.[9–15] Quite recently, attention has been given to the possibility of driving the interactions through specific shapes of the building blocks to be assembled,[16–19] thus mimicking the behavior of atoms and molecules with chemical bonds. Over the last decades, very powerful techniques for the characterization of small particles became available. Traditional attention has been given to the size or PSD, but (in several cases) it has also been recognized the important role played by particle shape (in several cases). Attention towards shapes has been initially given by people working with mineral powders and aerosols (e.g., clays). More recently, the same need has been transferred towards the characterization of engineered nanoparticles for an increasing number of applications. Regardless, the number of methods which are actually (suitable to) applicable for industrial applications is limited. Examples are small angle light scattering (SALS) and UV-VIS spectroscopy, which can be easily operated in line, but cannot measure dilute systems as often required by the industry.[20–26] All these methods recover data from a huge number of particles, which typically imposes the problem of data inversion, thus limiting the reliability of the methods especially when independent information about the sample is missing.[27]

Among the available methods, those measuring properties of single particles usually better fulfill the actual requirements especially for industrial application. Measuring single particles prevents from using inversion methods, and immediately enables to (the measuring of) measure highly polydisperse samples with peculiar PSDs. Microscopy techniques (optical, scanning electron microscopy, SEM, transmission electron microscopy, TEM, etc.; see Refs. 28–30 (as) for examples of applications), optical particle counter (OPC),[31–33] single particle obscuration sensor SPOS,[34] Coulter counters (see Ref. 35 for Coulter and a comparison among all these methods) are perhaps the most adopted for (in) a variety of applications. Microscopy methods and atomic force microscope (AFM),[36] often automated, represent by far the most powerful approach capable of characterizing size, shape, internal structure, and information about composition. Regardless, they are tremendously time demanding and often need specific sample preparation. Optical methods like OPC and SPOS are advantageous for being completely, non-invasive and easy to be operated in line. Ultimately (basically), the limit in the use of optical schemes is represented by the way the size is obtained from the optical signals, which could bring inaccurate results.[37] OPC measures the scattering cross section of particles from the power radiated within a wide solid angle. SPOS measures the extinction cross section from the power reduction of the beam transmitted downstream of the region where the particle traverses the beam. Both cross sections are determined by particle size, but the influence of composition, internal structures, shape, and orientations plays a role which in principle cannot be neglected to achieve the results with the precision required.[38] There is no way to overcome this limitation without introducing independent information about each particle. These instruments provide an "optical" size for each

a)Author to whom correspondence should be addressed. Electronic mail: marco.potenza@unimi.it

particle, which is the size of a sphere composed by a given material which would produce the same scattering properties of the measured particle, with a given composition, structure, shape, and orientation.[35,39–44] As a result, when in-line application is not the actual need, the optical methods are often not really appreciated in favour, for example, of the Coulter method which represents a benchmark for the sizing of particles in many fields. Again, in Coulter counters the shape of the particle is inaccessible, the size being measured on the basis of the particle volume thus obtaining a volume equivalent size people are well used to work with. Notice that the volume equivalent size is independent of shape and orientation, this being the huge advantage of the Coulter data from one side. On the other side, the lack of shape information is of great importance when the exploitation of the results of the Coulter measurements (is needed) to derive other parameters of the particles. This occurs, for example, when comparing Coulter measurements to OPC or SPOS ones, which cannot be reliably cross-calibrated.[34] This can be easily inferred by considering the effect of shape on volume equivalent radii.[35]

The possibility of gathering additional information beyond the size of single particles has been recently explored in connection with the possibility of measuring independently two parameters from the field scattered in the forward direction by single particles illuminated by a laser beam.[45] Here, we focus on the determination of size and shape by exploiting the novel single particle extinction and scattering (SPES) method, which recently proved to be suitable for applying the forward scattered field approach.[46] The method really takes advantage of the features which typically limit traditional techniques, such as sample polydispersity and strong dilutions. Fast and accurate characterization is then possible as described in Ref. 47 for the case of real suspensions of industrial interest. Here, we further extend the potential of this method by capitalizing on the specific features of the fields scattered by non-spherical particles with preferential orientations, a condition obtained by imposing proper shear conditions within the sample cell. A huge benchmark of results of accurate numerical simulations has been developed to quantitatively support data interpretation (Section III B and Appendix A).

II. EXPERIMENTAL APPROACH

A. Single particle extinction and scattering

Here, we just recall the basic elements of the experimental approach we use to extract the complex scattered field components through the SPES method, referring to published works for further details.[46–49] We exploit a self-reference interferometric scheme in which single particles are driven by a uniform, laminar flow at a given speed through a tightly focused laser beam. The (faint) scattered and the (intense) transmitted light interfere onto a segmented sensor in the far field of the laser beam, exploiting a condition which is similar to in-line holography.[50,51] The *intensity* modulations are proportional to the scattered field *amplitude*, thus realizing the so called optical heterodyne condition[52] that allows the measure of the amplitude and phase of the scattered fields. The self-reference scheme automatically provides an intrinsic calibration of the signals allowing the description of phenomena without any free parameter. In force of the Optical Theorem,[53,54] the real part of the forward scattering amplitude is obtained from the total extinction cross section. On the other hand, thanks to the self-interference conditions, the intensity modulation depth is determined by the amplitude of the field scattered forward, which allows to determine the imaginary part of the field amplitude. Accessing two independent, absolute measurements of the scattering fields represents the key advantage to extract additional information about the particles. More precisely, the polydisperse size distribution allows the extraction of precise information from the SPES measurements on a huge number of particles.[46–49] Measuring the refractive index, internal structure, aggregation state of the particles becomes accessible from the statistical analysis of the data in the complex field. As detailed in Section III, we will here extend the complex field approach to the case of nonspherical particles.

B. Samples

We analyze water suspensions composed by well characterized nonspherical particles: monodisperse, calibrated dumbbells composed by two spheres in contact, joint by a belt,[19] kindly provided by Peter Shall (University of Amsterdam); polydisperse, standard monophasic mineral samples: standard quartz (Merck) and kaolinite (Georgia Kaolin Co.). Finally, we show the results obtained by mixing the above mentioned quartz with illite (Tokaj region, northern Hungary). Dumbbells are composed by two PMMA spheres stuck together, so that the refractive index of the system is 1.49 in vacuum. They have been accurately characterized at optical microscope, obtaining an average diameter for the spheres of $1.7\,\mu m \pm 0.1\,\mu m$. Estimates of the refractive index of the mineral samples have been obtained through the measurements performed at optical microscope by matching the refractive index of the particles and the surrounding liquid (Cargille Refractive Index Liquids). All these samples have been accurately characterized in the past through SEM, XRD, and TEM.[55] In the Appendix E, we report examples of the results of SEM measurements performed exactly on the same samples measured with the SPES in this work, prepared by filtering the liquid and by covering the sample with a Gold conductive layer.

C. Orienting particles in the fluid flow

The breakthrough here is capitalizing on the knowledge of the particle orientation within the laser beam. We achieve this condition by injecting liquid through a cell thin enough to impose a stress orienting particles. A Hellma flow cell with rectangular section of $0.2 \times 3\,mm^2$ has been used. In our flow conditions (some cc/s), the Reynolds number of the cell is low enough to guarantee pure laminar flow, and rotational diffusion is absolutely negligible during the time spent by a particle in the light beam due to the high rotational Peclet number.[56] Therefore, the system is dominated by the velocity gradients within the cell. The flow can be roughly described as a Poiseuille flow with a parabolic velocity

profile in the thinner direction (neglecting the velocity profile in the other direction), where the velocity gradient is of the order of magnitude of $10^4 s^{-1}$. A preferential orientation along the velocity direction is then obtained after a particle moves over a length much smaller than the cell.[57]

When oriented along the streamlines, oblate and prolate particles behave very differently: prolates will be preferably oriented with the major axis within the plane transverse to the optical axis, z, so that light will mainly pass through the smallest thickness of the particle; oriented oblate particles, on the contrary, will maintain uniform probability of exhibiting major and minor axes along the light beam direction, thus spreading the average optical thickness appreciably with respect to the prolate case.

In order to support the effectiveness of the shear in orienting particles as described above, we performed measurements with a water suspension of dumbbells. This experiment represents a reference to prove the ability of our method to give proper orientation to non-spherical particles within the size range of interest here. In Appendix B, we report experimental results obtained with this sample, as well as a comparison to the measurements performed with a cell which does not impose any preferential orientation to the particles.

III. THEORY

In Section III A, we discuss the novel approach in terms of simplified, analytical arguments, to give a clear and simple guide for the data interpretation and analysis. We then address the case of real, polydisperse suspensions of several types of particles with different orientations through accurate numerical simulations in Section III B. In particular, we will focus on describing the effects of preferential orientations, such as those imposed by our experimental apparatus. More than 10^6 particles have been simulated in order to create a benchmark to be compared to data and to interpret the experimental results.

A. Extending the complex field approach

The knowledge of two independent parameters ultimately related to the real and imaginary parts of the dimensional scattering amplitude $S(0)$ in the forward direction ($\theta = 0$) by single particles drastically improves the capability of recovering information, thus introducing a completely novel approach for the analysis of small particles.[45] In connection with the SPES method,[46] this approach really becomes a breakthrough, since the complex fields scattered by single particles can be measured in liquid suspensions and the novel approach can thus be exploited. Nevertheless, the set of properties determining the field scattered by a particle cannot be rigorously recovered. Different combinations of properties can determine the same scattered field: there is no one-to-one relation between $S(0)$ and the set of properties. Even if particle size is usually considered as the most important parameter in determining the scattered field, particle composition, internal and surface structure, shape and orientation also affect the scattering properties.[44,58–62] Size and refractive index can be accurately obtained through the SPES method for single particles endowed with spherical as well as isometric shape.[47] More insight can be obtained through statistical analysis of the results obtained from many particles.

We recall that in the limit case of extremely small particles (Rayleigh scattering), or even for larger particles with small values of the relative refractive index (Rayleigh-Gans scattering), the scattered field amplitude can be approximated by a first order imaginary term and a second order real one.[53,54] Ultimately, measuring the imaginary part of the scattered field corresponds to measure its amplitude, which once squared gives the scattered intensity measured with traditional techniques adopted to measure the particle size, a. This is the approach exploited in the instruments like the OPCs. On the other hand, the real part is directly related to the total extinction cross section, C_{ext} (including both scattering and absorption), thanks to the so called Optical Theorem. We will follow the approach introduced by Van de Hulst[53] (see Ref. 53, p. 184) to describe the scattered field emerging from a generic structure by evaluating the field in a plane just downstream the scatterer. For simplicity, we will here consider the case of purely dielectric particles, which is enough for describing the suspensions which will be further analyzed.

Fig. 1 schematically represents the geometry of the system. The light impinges along the z direction and the object introduces amplitude and phase modulations in the transverse $\xi - \eta$ plane. The shape of the object is described by the thickness $t(\xi, \eta)$, and the refractive index relative to the surrounding medium being m. The deflection of light inside the particle is assumed to be negligible, an assumption which holds until precise conditions are met (see Van de Hulst[53] for extensive discussion of this assumption). Therefore, the field is only affected by phase modulations imposed by the optical thickness $\tau(\xi, \eta) = t(\xi, \eta)(m - 1)$ encountered by the impinging beam along any straight line with coordinates (ξ, η) drawn through the particle. The generalization for the case of a refractive index depending on the position is straightforward. The phase modulations imposed to the electric field are then given by

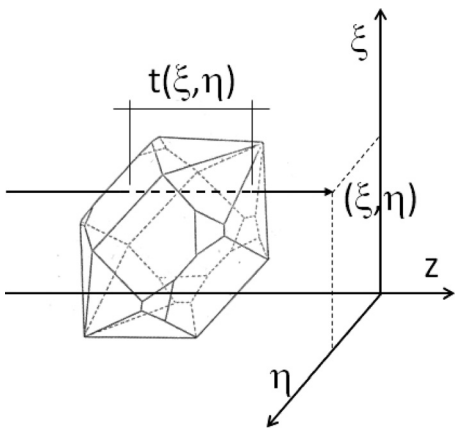

FIG. 1. A schematic representation of the system described in the text. The light impinges from the negative z direction. The particle is described by thickness $t(\xi, \eta)$ and relative refractive index m. The field is evaluated on the $\xi - \eta$, z = 0 plane.

$$\frac{k^2}{2\pi}[1 - e^{-ik\tau(\xi,\eta)}]. \quad (1)$$

Here $k = 2\pi/\lambda$, where λ is the light wavelength and i is the imaginary unit. By integrating the phase shifts over the cross section of the particle, Σ, the amplitude of the forward scattered field $S(0)$ is obtained

$$S(0) = \frac{k^2}{2\pi}\int\int_{\Sigma}[1 - e^{-ik\tau(\xi,\eta)}]d\xi d\eta. \quad (2)$$

Under the hypothesis of small optical thickness, $k\tau(\xi,\eta) \ll 1$, we expand the exponential in power series. At the second order of the expansion, the forward scattered amplitude $S(0)$ turns out to be given by the sum of two terms that are the imaginary and the real parts

$$S(0) = i\frac{k^2}{2\pi}\int\int_{\Sigma}k\tau(\xi,\eta)d\xi d\eta + \frac{k^2}{4\pi}\int\int_{\Sigma}k^2\tau^2(\xi,\eta)d\xi d\eta. \quad (3)$$

For the sake of completeness, we here stress that the result obtained in Eq. (3) can be interpreted in terms of two clear physical parameters. Under the same hypotheses that have been used here, and by introducing the Lorentz-Lorenz formula to relate the refractive index m to the polarizability of the molecules composing the particle, it is straightforward to identify the first term with $ik^3\alpha_{ptc}$, where α_{ptc} is the particle polarizability. This is rigorously the result for small particles. Even more easily, in force of the Parseval's identity the latter term in Eq. (3) gives the extinction cross section C_{ext} of the particle, multiplied by $4\pi/k^2$ as required by the Optical Theorem.

We introduce the average optical thickness of the particle at the given position

$$\tau_0 = \frac{1}{\Sigma}\int\int_{\Sigma}\tau(\xi,\eta)d\xi d\eta. \quad (4)$$

So that optical thickness can be split as

$$\tau(\xi,\eta) = \tau_0 + \delta\tau(\xi,\eta), \quad (5)$$

where $\delta\tau(\xi,\eta)$ is zero-averaged. By introducing the quadratic average of the fluctuations

$$\langle\delta\tau^2\rangle_{\Sigma} = \frac{1}{\Sigma}\int\int_{\Sigma}\tau^2(\xi,\eta)d\xi d\eta - \tau_0^2, \quad (6)$$

we can write the forward scattering amplitude as

$$S(0) = i\frac{k^3}{2\pi}\tau_0\Sigma + \frac{k^4}{4\pi}\tau_0^2\Sigma + \frac{k^4}{4\pi}\langle\delta\tau^2\rangle_{\Sigma}\Sigma. \quad (7)$$

The imaginary part, which will be denoted as I, is proportional to the average optical thickness τ_0 of the particle. Notice that the approach here adopted determines different τ_0 for different orientations and shapes, as discussed below in more detail. The real part of $S(0)$, R, splits into two parts: (1) a contribution related to τ_0 and (2) a contribution depending on how the optical thickness changes over the particle section, Σ, that is the feature described by the quadratic average of $\delta\tau(\xi,\eta)$.

The complex amplitude mainly depends on the particle size as mentioned above, other features just slightly affecting the results when represented in the complex plane. Especially for highly polydisperse samples, representing data in the complex plane partially hides the features we are interested in here. We then introduce a combination of parameters which evidences the main physical quantity here, namely, the optical thickness of the particle. We thus introduce the ratio

$$\rho = \frac{2R}{I} = \tau_0 k + \frac{\langle\delta\tau^2\rangle_{\Sigma}}{\tau_0}k = \rho_0 + \frac{\langle\delta\rho^2\rangle_{\Sigma}}{\rho_0}, \quad (8)$$

where we have posed $\rho_0 = \tau_0 k$ and $\delta\rho = \delta\tau k$ (following Van de Hulst[53]).

These expressions suggest that ρ exhibits actually the influence of (1) the average refractive index and (2) internal structures, irregular shapes, non-uniform compositions, etc. Indeed, the average refractive index determines ρ_0 for any particle. The other properties mentioned in item (2) affect both ρ_0 and $\delta\rho(\xi,\eta)$. In terms of representing experimental data, we therefore show plots of ρ as a function of C_{ext}. This choice is dictated by two main reasons: (a) C_{ext} is determined with much less uncertainty because of the specific properties and implementation of the SPES method;[46] (b) it is a monotonic increasing function of size (anyhow "size" is defined). In Fig. 2, we show examples of this representation for the fields obtained on the basis of Eq. (1) in the case of polydisperse cubes with two orientations: faces parallel to the optical axis (squares) and rotated by 45° around the x axis (diamonds). These results are compared to the spheres obtained on the basis of the Van de Hulst formulas (circles). Refractive indices $n = 1.53$ and $n = 1.58$ in water have been considered (open and solid symbols, respectively). Notice that squares always exhibit lower ρ, according to the vanishing value of $\langle\delta\rho^2(\xi,\eta)\rangle$ due to the plane parallel geometry.

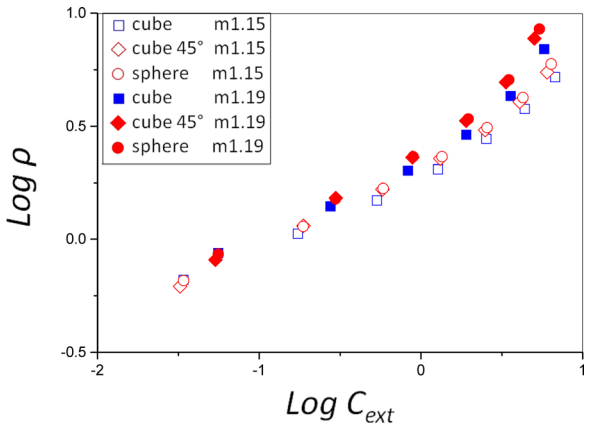

FIG. 2. Complex amplitudes for different cases of interest are represented in the $\rho - C_{ext}$ plane introduced in the text. Polydisperse cubes with two orientations (squares and diamonds, see text), compared to spheres (circles), are obtained for refractive indices $n = 1.53$ and $n = 1.58$ (open and solid symbols, respectively). Water suspension is considered here, with relative indices $m = 1.15$, $m = 1.19$.

B. Numerical simulations

We present the results of accurate numerical simulations performed with non-spherical particles which allow to (1) extend the range of applicability of the results obtained above and introduce the criteria to recognize different shapes, thanks to the preferential orientation of the particles as experimentally exploited below; (2) recover information from experimental data on the basis of precise computation of the field amplitudes in the cases of real interest, where analytical computation is realistically not viable, if not impossible. For simulating the scattered amplitudes of non-spherical particles, we exploited the Discrete Dipole Approximation, introduced long ago in astrophysics for similar purposes.[63,64] DDA is a very general method for calculating scattering from a particle of a given geometry and composition. The basic idea is to divide the particle into small cubical domains, and to replace them by point-like dipoles. The interactions between dipoles are then calculated numerically on the basis of the integral equation for the electric field. For an extensive review of the issues dealing with the practical implementation of the integral equations, see Refs. 65 and 66. More precisely, we adopted the Amsterdam Discrete Dipole Approximation (A-DDA) code,[67] developed in C since 1990 by Hoekstra and co-authors.[68,69] The code has been compared to other numerical codes.[66]

In order to compare the results for different shapes, and to extract the information for analyzing the experimental data, we adopt volume equivalent radii. The best way to introduce equivalent radii for particles of different shapes is questionable,[35,70–72] and ultimately depends on the specific application. Volume equivalence is one of the most common choices, even if it is not straightforward to compare the results with methods like OPC,[72] SPOS,[73] and Coulter. The differences among the results of these methods are ultimately due to the effects of shape and orientation of particles which affect optical measurements.[40,74]

Simulations have been performed for particles with different shapes and sizes to cover the entire range of sizes of the measured samples. Reference shapes are considered to be ellipsoids, cylinders, and hexagonal prisms, with oblate and prolate shapes. In order to give a clear distinction between prolate and oblate particles, the aspect ratio is defined to be smaller than 1 for oblate, larger than 1 for prolate, being defined as the ratio between the smaller size divided by the larger for the oblate case, and the larger size divided by the smaller for the prolate. We have chosen orientations which can be imposed experimentally, which are with the major axes along the fluid flow direction for oblates and the minor axis along the laser direction for prolates.

In Fig. 3, we present the results obtained for oblate particles with aspect ratio 0.2 and prolate particles with aspect ratio 5, refractive index $n = 1.55$. Plots are 2D histograms where the color scale indicates the number of events in each 2D bin, normalized to the maximum value in the plot (yellow = 0, blue = 1). Insets just give a couple of examples of the imposed orientation. Red lines indicate the laser beam direction and blue lines indicate the liquid flow. Ellipsoids, cylinders, and hexagonal prisms are considered, no

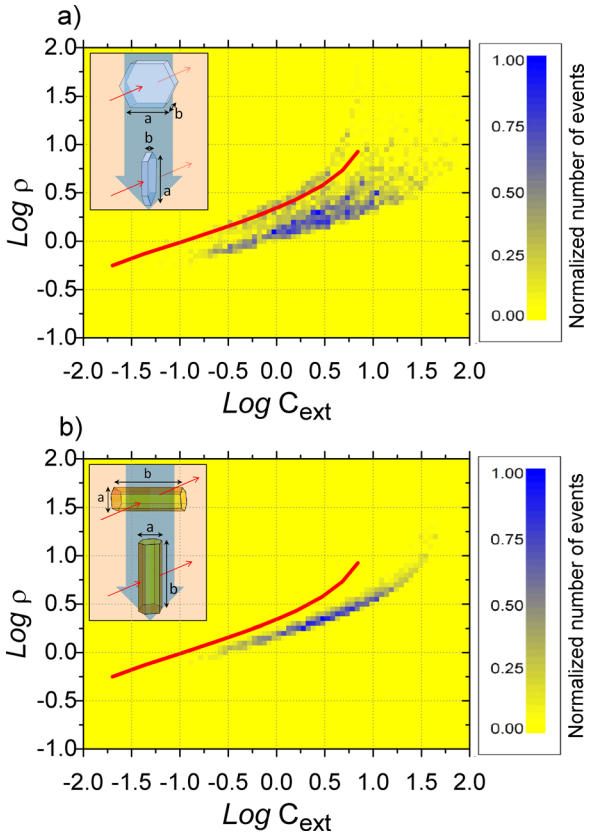

FIG. 3. Numerical results obtained for oriented oblate (a) and prolate (b) particles with aspect ratios 0.2 and 5, respectively, $n = 1.55$ suspended in water. Ellipsoids, cylinders, and hexagonal prisms have been considered here. Spheres are represented by the continuous (red) lines. The spread in the vertical direction characterizes the oblate case only. For prolate objects, the average optical thickness is appreciably different from the spherical case. Insets represent two particular cases in the range of orientations considered in the simulations (see text for details).

differences among them being appreciable here. As expected, an appreciable spread is present in the $\rho - C_{ext}$ plane along the ρ direction. In more detail, oblate particles apparently show a population composed by a main contribution on top of a more uniform structure spread into the plane. This is the effect of representing just one value of the aspect ratio. Extending the range of aspect ratios immediately smears out the results.

Prolate particles are clearly characterized by a narrow distribution in the vertical direction while the opposite is true for the oblate case, showing a wider dispersion of data in the vertical direction. Quantitatively speaking, we measure the spread in ρ by simply evaluating the standard deviation of the histogram obtained as a vertical section within a given C_{ext} range where noise is negligible (see Appendix C for details). We obtain 0.27 and 0.05 for oblate and prolate particles, respectively. In Appendix A, we report the results obtained for exactly the same samples with totally random orientations of the particles for comparison. Moreover, we stress that the population of prolate particles in the $\rho - C_{ext}$ plane is clearly distinguishable from that expected for spheres (or isometric particles) with the same refractive index (continuous lines). This is essential to decide for the prolate, oriented nature of these particles instead of the

isometric ones, once the refractive index is known even approximately. Even easier is the identification of oblate particle due to the broadening of the distribution. To be quantitative, for aspect ratios larger than 2–3, distinguishing isometric and non-isometric particles can be done by knowing the refractive index with 10%–15% uncertainty, which is a range broad enough to give a reasonable estimate. We stress that the case of prolate particles with a broad distribution of aspect ratios cannot in any case mimic the results obtained with oblates, since in no way prolate particles can overcome the line of spheres, as in the case of oblates.

We finally point out that our simulations only describe particles without any surface roughness, internal structure, complex shapes, etc. In force of the arguments discussed in Sec. III A, we conclude that these features will mainly introduce a further spread in the $\rho - C_{ext}$ plane, thus smoothing the structures which are observable in the results shown here.

IV. EXPERIMENTAL RESULTS

In this section, we present the results obtained with the samples described in Section II, and prove the capability of the method to recover shape and size distributions. First of all, we determined the transfer function of the instrument, which spreads data in the vertical direction especially at the lower sizes when the signal amplitude is smaller. Accurate measurements have been done to characterize this contribution with calibrated polystyrene and PMMA spherical particles of several diameters. We find a spread in the imaginary part described by a Gaussian function with a standard deviation of 3.5 imaginary units and an offset of 7. Thanks to the ultimate features of the measurement procedure adopted here, the complex amplitudes exhibit by far the main uncertainty on the imaginary part, I. The real part, R, is much more accurate, thanks to a better accuracy in determining C_{ext}.[46] Therefore, the representation in the $\rho - C_{ext}$ plane is essentially affected by noise mainly along the ρ (vertical) direction. As a result, convolving the numerical results with the transfer function measured experimentally is an easy task. On the contrary, de-convolving the experimental results for the transfer function is almost impossible, just because of the typical limitations encountered with ill-posed problems. Notice that de-convolving data here would need to be performed along each vertical line of pixels, which is intrinsically limited in terms of the number of measured events. We therefore extract information about the aspect ratios of the particles through proper look up tables (LUT) properly developed on the basis of the simulations presented above. We checked the method with a very well known dumbbell sample. The results are reported in Appendix D.

Fig. 4 represents SPES data obtained with quartz. Continuous line represents the expected results obtained on the basis of Mie theory for spheres with a distribution of sizes and the refractive index of quartz. There is an evidence that the population is narrowed and shifted as a result of orienting the particles. The standard deviation of the ρ distribution evaluated as discussed above turns out to be 0.06. According to what discussed above, we can guarantee that

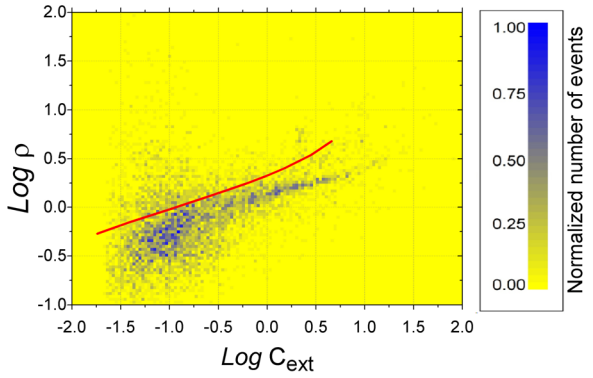

FIG. 4. SPES data for the polydisperse quartz powder suspension compared to the expected values for spheres with the quartz refractive index (continuous red line).

this is solely compatible with prolate shapes for that refractive index. This is in agreement with the expected shape of quartz.

Different results are obtained with kaolinite which is well known to be composed by platelets. In Fig. 5, the population is appreciably broadened in the vertical direction, in accordance with the oblate shape, with a standard deviation for ρ of 0.17. We notice that in comparison to the numerical results shown in Fig. 3, experimental data show a different ρ distribution. This discrepancy is simply due to the single value of the aspect ratio adopted in Fig. 3. Extending the aspect ratio range immediately smears out the population in the two dimensional plots in a similar way as obtained from the measurements.

Moreover, there is no doubt whether this spread could be due to a distribution of the aspect ratio. This has been accurately verified by mixing the results of numerical simulations of prolate particles with a range of aspect ratios from 1 to 10. The resulting spread in ρ is not enough extended at the lower values. We also stress that for a given material it does not make too much sense covering ranges of aspect ratios extremely extended.

By exploiting the set of numerical simulations described in Section III B, we can recover the ARD and PSD through the procedure described in Appendix C. First, either the

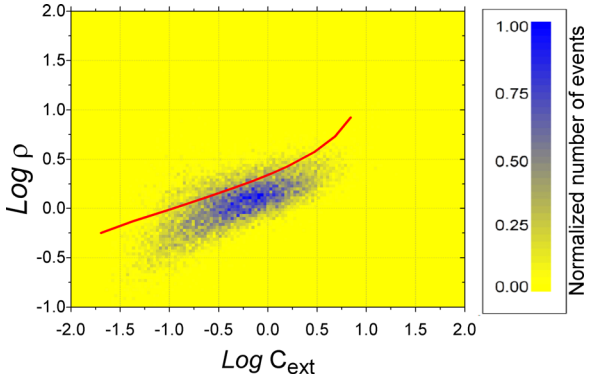

FIG. 5. SPES data for the polydisperse kaolinite powder suspension compared to the results expected for spheres with the refractive index of kaolinite (continuous red line).

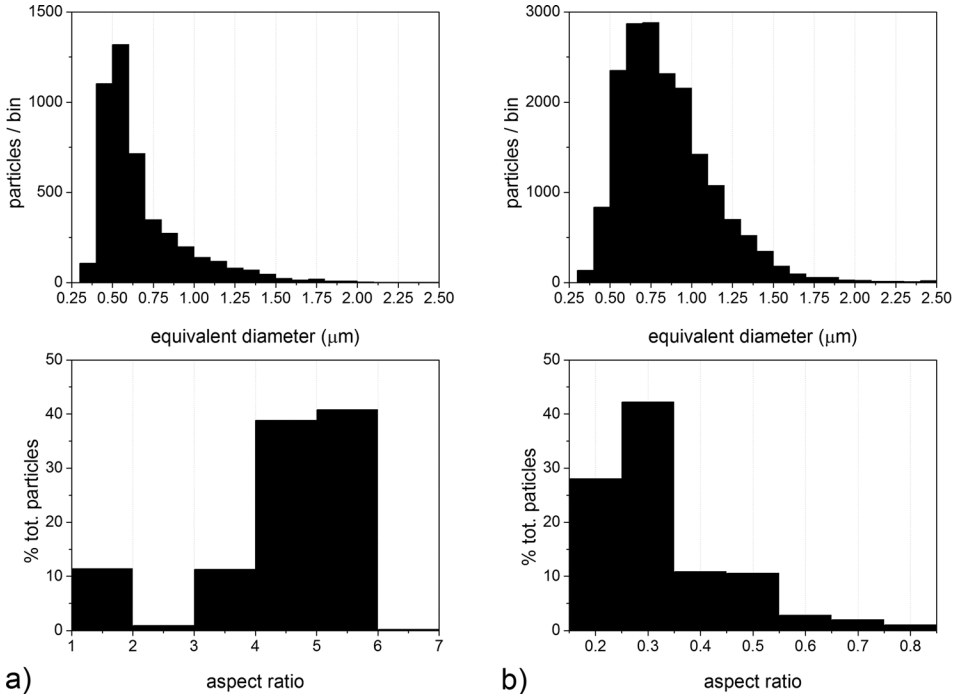

FIG. 6. ARD and PSD recovered for the quartz (a) and the kaolinite (b) samples.

oblate or the prolate shape has to be decided for by inspection of the data sets. Thanks to the knowledge of the refractive index we can then compare the measured $\rho - C_{ext}$ distributions to those obtained from numerical simulations as an additional check of the method. Fig. 6 reports the results obtained for the quartz and kaolinite samples, in terms of PSD and ARD.

As a further example of the capability of the method, we consider the measurements of a non-trivial sample composed by a mix of illite and quartz. Illite is well known to be very reactive,[75] and appropriate preparation procedures have been followed basing on typical dialysis methods like those described in Ref. 71 in order to destroy aggregates and to make the suspension stable enough. Notice also that after the strong dilution needed for performing the SPES measurements, the typical number concentration within the samples is low enough to exclude any aggregation of the particles.[76] The result of SPES measurements performed upon the dialyzed sample is plotted in Fig. 7(a). Two populations are evident. The upper one is very similar to that obtained above for quartz. One could wonder whether these populations could be either compatible with a suspension of isometric particles of different materials (which would give narrow populations as well), or with a suspension of prolate particles as above. Notice that because of the narrow distribution, it is simply impossible that particles are oblate. Unfortunately, a simple measurement of the refractive index is not so easy here due to the presence of two different species, and it is impossible to index matching the powder and the surrounding fluid. Nevertheless, if the two populations in the SPES data are inverted assuming spherical (or any isometric) shape, refractive indexes close to $n = 1.40$ and 1.37 are found, respectively, dramatically low for almost any compact particle composed by common materials. By contrast, interpreting the data due to prolate particles with the properties described above gives $n = 1.54$ for the upper population, and 1.42 for the lower one, consistent with the expected refractive index of illite. We therefore interpret the results as possibly due to the presence of prolate particles for both species. Independent analyses performed on the same sample, such as elemental SEM measurements and SEM imaging, confirmed the presence of both quartz and illite, both with preferable prolate shapes (see Appendix E).

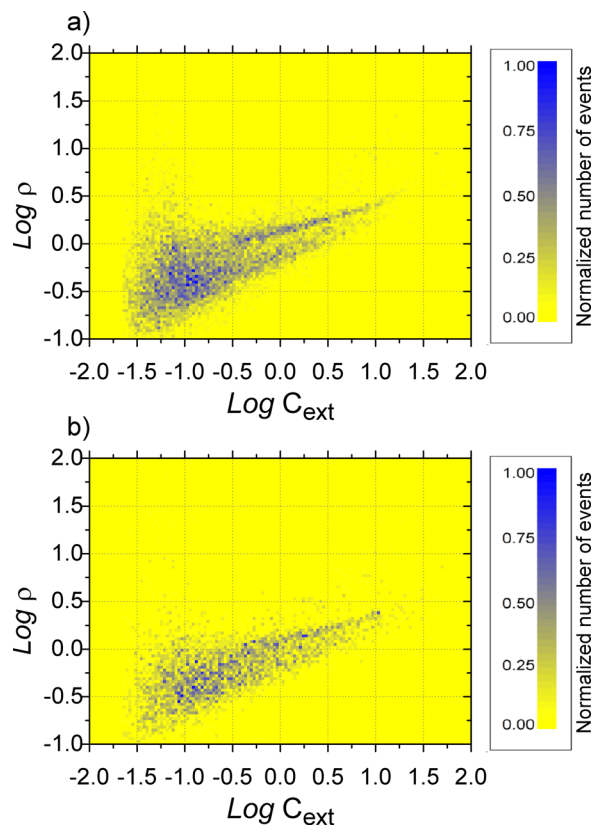

FIG. 7. SPES results obtained with a sample of illite. Results for stabilized (a) and non-stabilized samples are compared.

For the sake of completeness, in Fig. 7(b) we report the SPES data obtained with the non-dialyzed suspension. The results are compatible with the presence of both kinds of grains, and a population of grains with the intermediate optical properties, probably due to the presence of aggregates which have been destroyed with dialysis.

V. DISCUSSION

We have reported the possible advantages of operating with (1) the complex field approach[45] in connection with (2) the SPES method[46] and (3) the specific orientation of the particles passing through the scattering region (this work). Integrating these elements into one method brings a real breakthrough in characterizing single particles endowed with appreciably non-spherical shapes. The method takes advantage from the polydispersity of the sample and can be operated in flow. These elements make a substantial difference with traditional optical approaches, which are typically strongly limited by the spurious effects due to shape, orientations, and polydispersity.

We have shown that the independent knowledge of the sample is appreciably reduced with respect to traditional methods, being essentially limited to a rough estimate of the refractive index to exclude the peculiar case of isometric or spherical particles. For aspect ratios larger than approximately 2 (i.e., prolate particles), distinguishing isometric and non-isometric particles can be done by knowing the refractive index with 10%–15% uncertainty, which is indeed a very large range for most of the common materials. For oblate particles, the spread in the vertical direction makes the data interpretation slightly more difficult, because of the potential interpretation in terms of the effects of shape and index distribution. In fact, this limitation could be appreciably reduced by introducing LUTs based upon a more extended range of indices. Prolate particles with a broad distribution of aspect ratios can be rigorously distinguished from oblate particles since the former cannot in any case overcome the isometric line, whilst the latter do.

By listing the information that can be recovered, we have: (1) any broad population is compatible with oblate particles; (2) narrow populations are compatible with both isometric and prolate particles, but for different indices. Independent information about the refractive index, even an approximate value, can decide between the two cases; (3) PSD and ARD are both obtained on the basis of proper inversion algorithms based upon numerical simulations comparing with the data.

We stress that, thank to the approach we have adopted, which compares the numerical simulations to the experimental data, we access directly to the information about the geometrical aspect ratio, which is the one imposed in the simulations. This is an appreciable advantage.

The main limitation of the method is the need of working with diluted suspensions. Even if this can be considered also an advantage, in some cases this could limit the applicability. Examples are those cases in which changing the concentration can affect the properties of the particles, for example, emulsions. The number concentration of the samples measured here is of the order of 10^{-5} vol/vol, and a value of 10^{-4} vol/vol can be considered as an upper limit.

The method can be operated in any liquid, provided that the laser light passes through. Application to air or gases is also possible, even if in this case the conditions to orient particles change appreciably, this is mainly due to the different viscosities.

From the experimental point of view, the main limitation in the SPES data is represented by noise in the small C_{ext} range. This is mainly attributable to the fluctuations of the laser intensity, one cannot easily get rid of in the SPES device exploited for the measurements reported here. It is possible to operate with different optical layouts which allow to limit noise and the corresponding spread in the $\rho - C_{ext}$ plane, as it has been done, for example, in Ref. 47. Here, we have adopted the described version as a trade off to access precise information of both ρ and C_{ext} in the range exploited above for the data analysis, still maintaining the sizing data for the smallest sizes.

Performing a measurement requires approximately 10 min (depending on concentration). This is a long time if compared to traditional SALS and OPC measurements, but can be considered incomparably shorter than the time needed for performing a corresponding analysis with any microscopy device to measure a comparable amount of particles.

VI. CONCLUSIONS

We have shown the possibility to recover the information about shape on the basis of the simple and robust optical method of SPES, thanks to a novel methodological approach relying on the complex scattered field. Characterizing the shape of the particles has an overwhelming importance in science and industry, for example, in the widespread realm of clays. Clays have unique properties as materials, many of them related to their shape only, which is systematically determined by the important characteristics of interest for applications. The ability of absorbing, retaining, releasing a number of ions or molecules, for example, comes from unique properties of these materials, which in turn determine their shape. More generally, huge interest is given nowadays to characterize micro- and nano-sized colloidal materials in view of the so called bottom-up approach. A specific, precise knowledge of the shapes is of fundamental importance both from the geometrical and the physico-chemical point of view when small particles are used as ultimate "briks" to mimic what atoms do on the much smaller scale of atomic bonds.[17,19,77–79]

On the other hand, the knowledge of shapes is of paramount importance in aerosol science, where shapes are currently accessed through LIDAR only for the airborne particles. Methods for measuring particles collected on filters or any other solid substrate have the same drawbacks described above for the analysis of solid samples. As a result, SPES could be the ideal method to be exploited in air flow, to directly measure the optical properties of airborne particles. These applications could open new vistas on the complex issue of radiative transfer through the atmosphere.

Also, the characterization of dust particles from ice cores could take advantage from the SPES measurements of oriented particles. We have performed a preliminary study for the characterization of the water suspended particles from Antarctica ice cores,[82] which bring completely new information, complementary to any current characterization. By imposing the constraints imposed with the SPES measurements in water, the knowledge of the optical properties of airborne dust grains could be appreciably improved.

Finally, applications in the fields of accurate characterization of nanoparticles for industrial, medical, diagnostical applications could take huge advantage from a reliable measurement of the particle shape, with no need of any time consuming technique as imaging, or complicated light scattering methods which can be mainly exploited in research laboratories.

ACKNOWLEDGMENTS

We acknowledge Professor Guido Parravicini for supporting the fluidodynamics description of particles oriented by the shear flow. We acknowledge the anonymous referees for useful suggestions.

APPENDIX A: NUMERICAL SIMULATIONS

We here present the results of numerical simulations obtained with randomly oriented particles. Exactly the same collections of particles reported in the main text have been considered, so to compare the orientation effects only. In Figs. 8(a), 8(b), and 8(c), we present the results obtained for oblate particles with aspect ratio 0.2, refractive index $n = 1.55$, suspended in water, randomly oriented. Plots are 2D histograms where the color scale indicates the number of events in each 2D bin, normalized to the maximum value in the plot (yellow = 0, blue = 1). Ellipsoids (a), cylinders (b), and hexagonal prisms (c) are considered. Continuous lines describe the amplitudes expected for spheres having the same refractive index of the particles.

Similarly, Figs. 8(d), 8(e), and 8(f) show the results for prolate particles with aspect ratio 5, $n = 1.55$, suspended in water. Ellipsoids (d), cylinders (e), hexagonal prisms (f), and spheres (continuous line) are considered.

Differences are there in comparison to the experimental measurements. The reason of this apparent discrepancy is that here we only show the results obtained by fixing one

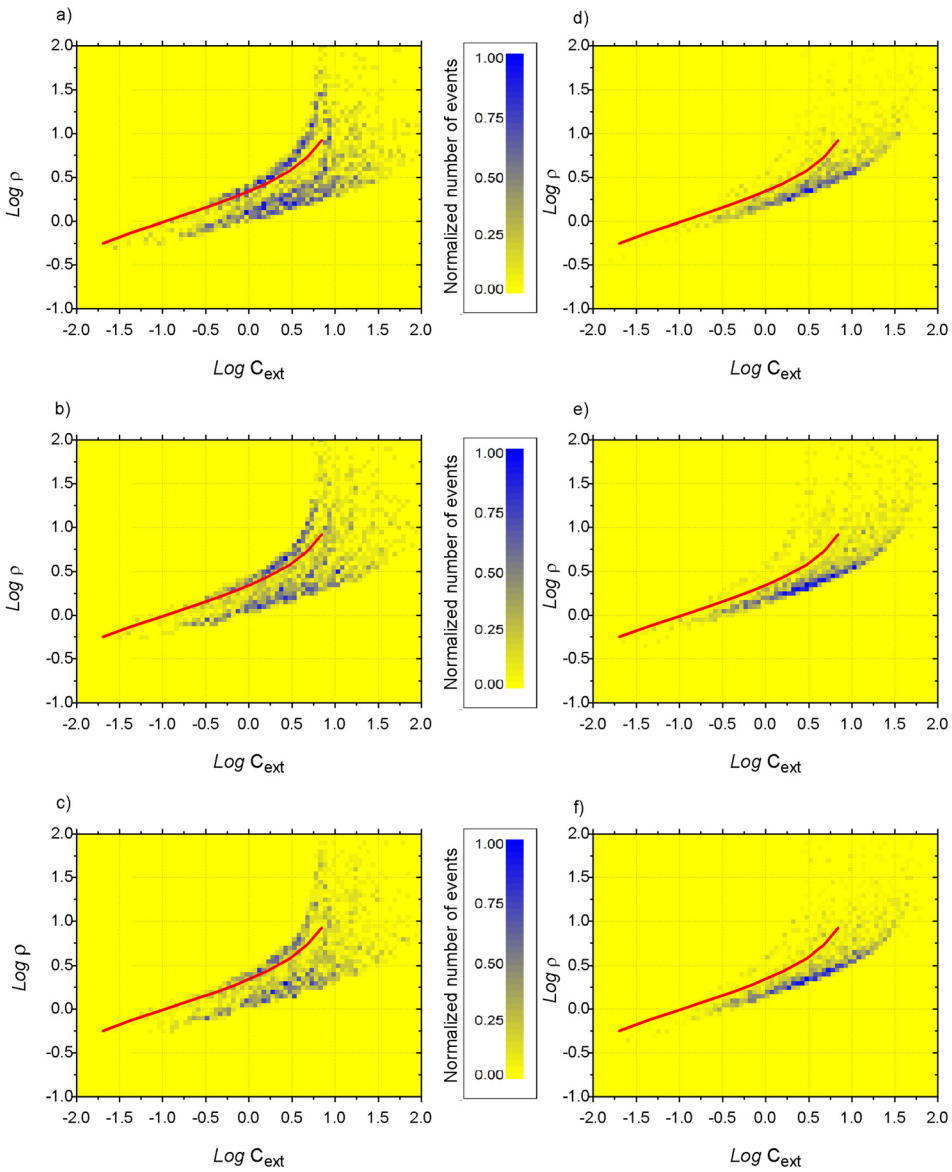

FIG. 8. Numerical results obtained for randomly oriented particles. Oblate ellipsoids (a), cylinders (b), hexagonal prisms (c) with aspect ratio 0.2; and prolate ellipsoids (d), cylinders (e), hexagonal prisms (f) with aspect ratio 5. Spheres (continuous lines) are also reported. Notice the spread in the vertical direction, induced by the random orientations of non-spherical particles.

value for the aspect ratio (0.2 for oblate and 5 for prolate). Notice that in Figs. 4 and 5 data are shown in the case of oriented particles in the real measurement conditions.

APPENDIX B: ORIENTING PARTICLES WITHIN THE FLUID FLOW

To prove the capability of the system of orienting particles into the flow cell, we show the results of measurements performed with two cells of different sections, one imposing a preferable orientation to the particles, the other does not. The former cell is thin along the direction of the laser beam, with a rectangular section $0.2 \times 3\,\mathrm{mm}^2$, the latter has a square section $1.5 \times 1.5\,\mathrm{mm}^2$. The water speed is 0.5 m/s and 0.1 m/s, respectively. In both cases, the Reynolds number of the cell is low enough to guarantee pure laminar flow. As mentioned in the main text, at least for the former cell rotational diffusion is absolutely negligible during the time spent by a particle in the light beam, due to the high rotational Peclet number.[49] Therefore, the system is dominated by the velocity gradients within the cell. The flow can be roughly described as a Poiseuille flow with a parabolic velocity profile in the thinner direction, where the velocity gradient is of the order of magnitude of $10^4\,\mathrm{s}^{-1}$. A preferential orientation along the velocity direction is then obtained after a particle moves over a length much smaller than the cell.[50] From a quantitative point of view, unfortunately the case of the square cell is impossible to be described by simple order of magnitude arguments like the previous ones, and a mathematical description is very difficult too. We just notice that the flux is slower, and the lower values of the shear Reynolds number of the particles make the orientational effects to be smaller.[80,81] We therefore cannot provide a specific receipt to estimate the conditions which guarantee particle orientation.

In order to better explore this issue, we performed measurements with the well known prolate particles. In Fig. 9, we report the SPES data obtained with the square section cell (a) and the thin cell (b) for suspensions of dumbbells particles as described in the main text. The difference is clear, since the distribution of ρ is vertically extended in the former case, very narrow in the latter. This is in accordance with our expectations of random orientations and almost totally aligned dumbbells, respectively. Spurious events are evident in the central region of the plot (a), while they are almost completely absent in (b). The other difference among the two data sets is the non negligible amount of events spread over an extended range of C_{ext} in case (a). This is a drawback of exploiting the thick cell, due to the particles passing through the beam outside the focal region, a condition which is rigorously prevented for in the thin cell since the focal region is longer than the cell thickness.

This contribution cannot be completely get rid of, and determines the presence of a small number of fake events introducing an extra population in a region corresponding to the sizes much smaller than the real ones. Nevertheless, as we will show further, these events can be easily recognized on the basis of the complete information available here.

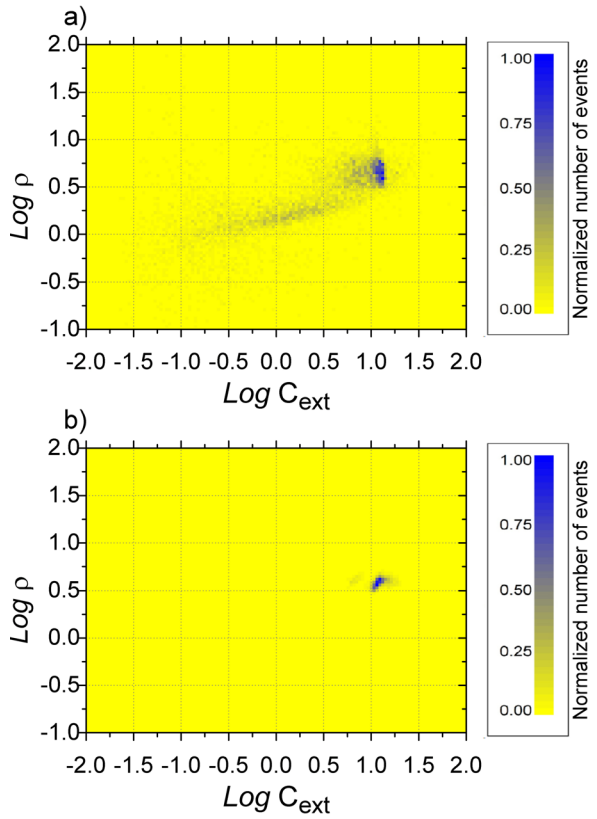

FIG. 9. Experimental results obtained for dumbbells without (a) and with (b) shear imposed by the flowing fluid. Vertical spread is present in (a), as expected. Spurious events are evident in (a), not in (b) as discussed in the text.

Finally, since the most complete and quantitative information comes just from the measurements performed with the thin cell, this is not an issue for our further measurements.

APPENDIX C: DETERMINATION OF ARD AND PSD

Here, we explain how we extract ARD and PSD from the experimental result of a typical polydisperse sample. Again, either oblate or prolate shape has to be decided for by the distributions of experimental data. To obtain the ARD and PSD, an approximate knowledge of the refractive index of the particles is needed, as discussed in the main text. Once the refractive index has been fixed, we extract a vertical section of the data set, which is a distribution of particle number as a function of ρ within a limited range of C_{ext}. This range is set in order to exclude the instrumental noise at the smallest sizes, and to maintain a reasonably large number of recorded events, which means excluding the largest particles. In Fig. 10(a), an example of such a section for kaolinite data is reported for C_{ext} comprised between 2 and 3.1 $\mu\mathrm{m}^2$ (histogram), that is, for $0.3 < Log\ C_{ext} < 0.5$. By fitting with a linear combination of distributions obtained from simulations with different aspect ratios (solid squares in Fig. 10(a)), we get the ARD. We can therefore proceed to build an LUT specifically aimed to extract the PSD for the particles with the given ARD and orientations. In Fig. 10(b), we report the LUT for the kaolinite sample measured here. The black line represents the 50% contour level of the experimental data

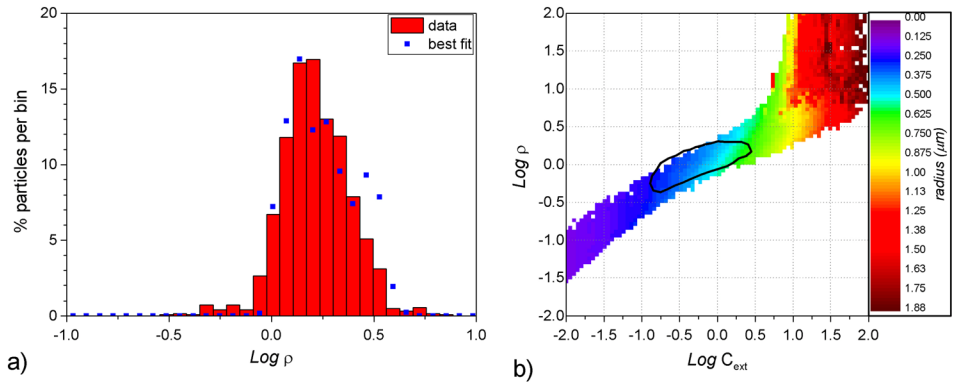

FIG. 10. (a) An example of the best fitting (solid squares) to measure the ARD for the kaolinite sample. (b) The LUT obtained from the ARD recovered in (a), where the color scale indicates the radii as detailed in the legend. The black line is the 50% contour level of the population reported in Fig. 5.

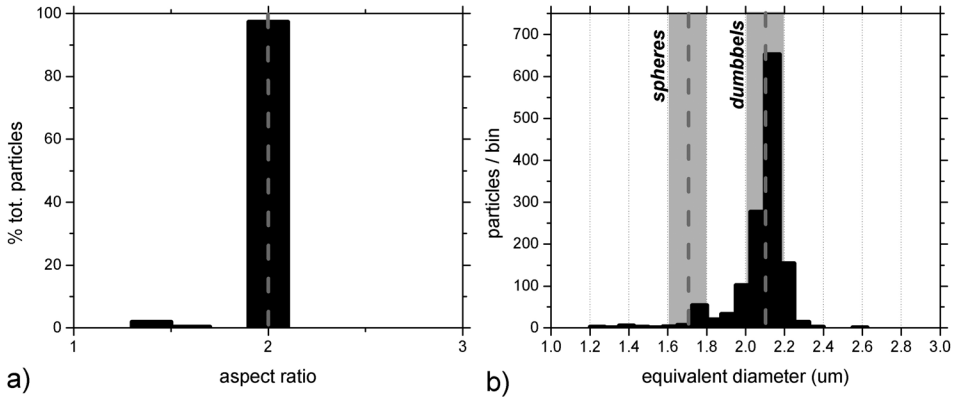

FIG. 11. ARD (a) and PSD (b) histograms obtained from the measurements with the thin cell, reported in Fig. 9(b). In (a) dashed grey line indicates the expected value for the ARD. In (b) dashed lines and gray columns, respectively, represent the average and standard deviation for spheres and dumbbells.

plotted in Fig. 5. It is evident that the C_{ext} range chosen above guarantees the noise to be negligible, and the LUT can be exploited properly. Notice that we are assuming here a uniform distribution of the ARD for different sizes, which is considered to be reasonable enough in this range of sizes for mineral dust.[28,44]

APPENDIX D: CHARACTERIZATION OF DUMBBELLS

As an example of this approach, we show the results obtained for dumbbells (see Fig. 10(b)). The prolate shape can be recognized on the basis of Fig. 10(b). The refractive index is known ($n = 1.49$ in vacuum). We extract a vertical section of the data set, which is a distribution of particle number as a function of ρ. This section is then fitted by a linear combination of corresponding vertical distributions obtained from simulations with different aspect ratios. On this basis, each event in Fig. 9(b) can be associated to the corresponding size, to obtain the PSD of the sample. In Fig. 11, we represent the ARD (a) and the PSD (b) for the dumbbell sample. Black histograms are compared to the expected values (dashed vertical lines). Gray columns represent the standard deviation from the average for both spheres and dumbbells as obtained from optical microscopy measurements.

The results shown in Fig. 11 are in good accordance with the geometrical parameters of these particles, namely, an aspect ratio of 2 (two spheres stuck together) and a volume equivalent diameter of 2.1 μm (see the vertical dashed lines).

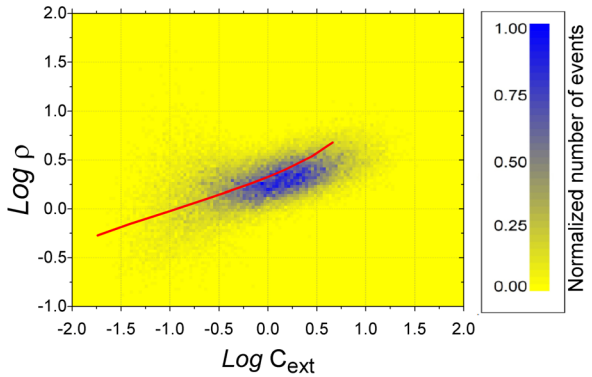

FIG. 12. SPES data for the polydisperse quartz powder suspension without orienting particles. The difference in the vertical broadening is evident with respect to the results obtained with preferential orientation (see Fig. 4). Red line represents the fields expected for ideally spherical quartz particles.

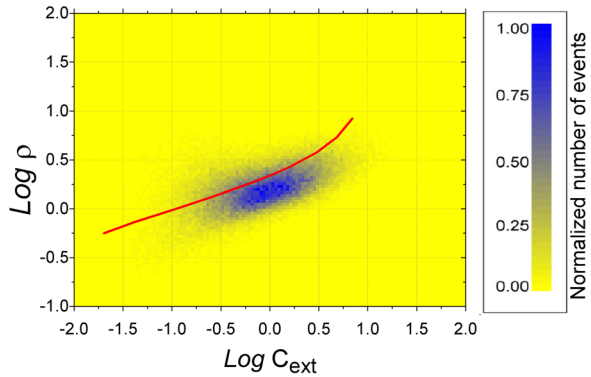

FIG. 13. SPES data for the polydisperse kaolinite powder suspension without orienting particles. The vertical broadening is essentially the same as that obtained with the thin cells (see Fig. 5). Red line represents the fields expected for ideally spherical quartz particles.

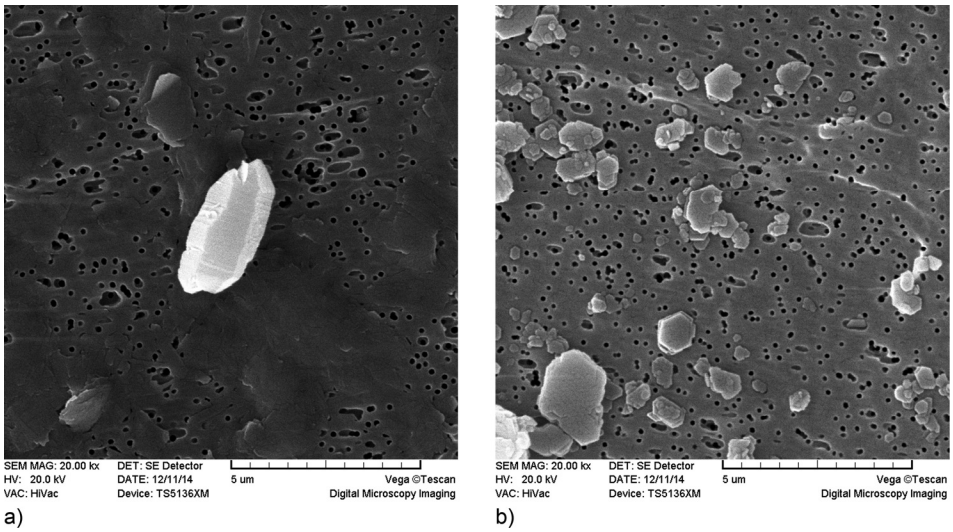

FIG. 14. Example of the SEM images obtained for the quartz (a) and kaolinite (b) powders considered here.

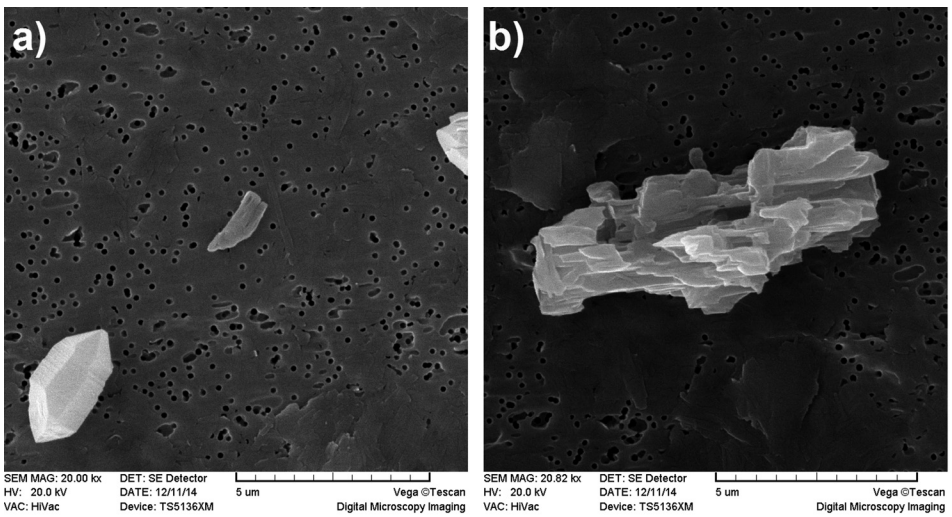

FIG. 15. SEM images of typical grains in illite-quartz sample. In (a) quartz is present. In (b) the non-compact, layered structure of illite grains is evident.

APPENDIX E: ADDITIONAL RESULTS

Here, we report a couple of additional SPES measurements performed with the thick cell on the samples described above, which prevents the samples from being preferentially oriented. We also report examples of the images obtained at SEM on the same samples measured with the SPES, prepared by filtering the liquid and by covering with a Gold conductive layer.

Figs. 12 and 13 report SPES data obtained with quartz and kaolinite, respectively, without any preferable orientation. Continuous lines represent the expected amplitudes obtained on the basis of Mie theory for polydisperse spheres with the refractive index of quartz. There is evidence that the population is broadened in the vertical direction, according to the presence of non-spherical, randomly oriented particles. Comparing to data in Fig. 4, a difference is found in the left-hand side of the plots. This is due to the particles passing through the beam outside the focal region, which determine spurious signals as discussed for the dumbbells case. At variance with the monodisperse case of dumbbells, here the sensibility to the smallest particles which originates smaller signals is reduced because of medium and large particles traversing the beam out of the sensible region, thus determining signals hiding any small signals from smaller particles.

SEM images have been acquired for the quartz, kaolinite, and the mixed illite-quartz suspensions. Moreover, elemental SEM measurements confirmed the presence of both quartz and illite, as expected. Here, we report a few images among the number collected at SEM. In Fig. 14, we report typical images for quartz (a) and kaolinite (b). Fig. 15 reports two images obtained with the quartz illite mixing. Both images are compatible with prolate shapes in accordance with the SPES measurements. In (a), the presence of both species is evident. Furthermore, the layered structure of illite grains explains the low (average) refractive index of the whole grain measured from SPES data. Notice, however, that we base our assessments about shape over independent knowledge of the samples.[55]

[1]J. C. Santamarina and G. C. Cho, in Proceedings of the Skempton Conference, London, 2004.
[2]M. C. Roco, C. A. Mirkin, and M. C. Hersam, J. Nanopart. Res. **13**, 897–919 (2011).
[3]A. A. Keller, S. McFerran, S. A. Lazareva, and S. Suh, J. Nanopart. Res. **15**, 1692 (2013).
[4]S. E. Pratsinis, AIChE J. **56**, 3028–3035 (2010).
[5]J. Scheckman, P. H. McMurry, and S. E. Pratsinis, Langmuir **25**, 8248–8254 (2009).
[6]M. T. Swihart, Curr. Opin. Colloid Interface Sci. **8**, 127–133 (2003).

[7]J. Park, K. An, Y. Hwang, J.-G. Park, H.-J. Noh, J.-Y. Kim, J.-H. Park, N.-M. Hwang, and T. Yeon, Nat. Mater. **3**, 891–895 (2004).
[8]A. Zelenyuk, L. Cai, and D. Imre, Aerosol Sci. Technol. **40**, 197–217 (2006).
[9]See www.itrs.net for ITRS Industry Goals for Particle Measurements in UPW and Liquid Chemicals, ITRS Yield Enhancement 2009 Edition.
[10]Y. Li, *Microelectronic Applications of Chemical Mechanical Planarization* (Wiley and Sons, Hoboken, 2008).
[11]K. Pate and A. Tregub, in 2011 International Conference on Power Transmissions.
[12]G. B. Basim, J. J. Adler, U. Mahajan, R. K. Singh, and B. M. Moudgil, J. Electrochem. Soc. **147**, 3523–3528 (2000).
[13]G. B. Basim and B. M. Moudgil, J. Colloid Interface Sci. **256**, 137–142 (2002).
[14]D. DeNardis, H. Choi, A. Kim, M. Moinpour, and A. Oehler, *Investigating the Effects of Diluting Solutions and Trace Metal Contamination on Aggregation Characteristics of Silica-Based ILD CMP Slurries* (Mater. Res. Soc. Symp. Proc., 2005), Vol. 867.
[15]S. Ghosal, P. K. Weber, and A. Laskin, Anal. Methods **6**, 2413–2792 (2014).
[16]S. J. Veen *et al.*, PRL **109**, 248302 (2012).
[17]S. Sacanna and D. J. Pine, Curr. Opin. Colloid Interface Sci. **16**, 96–105 (2011).
[18]L. Rossi, S. Sacanna, W. T. M. Irvine, P. M. Chaikin, D. J. Pineb, and A. P. Philipse, Soft Matter **7**, 4139–4142 (2011).
[19]Y. Wang, Y. Wang, D. R. Breed, V. N. Manoharan, L. Feng, A. D. Hollingsworth, M. Weck, and D. J. Pine, Nature **491**, 51–55 (2012).
[20]B. H. Zimm, J. Chem. Phys. **16**, 1093–1099 (1948).
[21]B. H. Zimm, J. Chem. Phys. **16**, 1099–1116 (1948).
[22]P. J. Wyatt, Anal. Chim. Acta **272**, 1–40 (1993).
[23]C. C. Gravatt, Appl. Spectrosc. **25**, 509–516 (1971).
[24]J. Cornillault, Appl. Opt. **11**, 265–268 (1972).
[25]F. Ferri, M. Giglio, E. Paganini, and U. Perini, Europhys. Lett. **7**, 599–604 (1988).
[26]D. Dudášová, S. Simon, P. V. Hemmingsen, and J. Sjöblom, Colloid Surf., A **317**, 1–9 (2008).
[27]O. Muñoz, H. Volten, J. W. Hovenier, B. Veihelmann, W. J. van der Zande, L. B. F. M. Waters, and W. I. Rose, J. Geophys. Res. **109**, D16201, doi:10.1029/2004JD004684 (2004).
[28]J. S. Reid, H. H. Jonsson, H. B. Maring, A. Smirnov, D. L. Savoie, S. S. Cliff, E. A. Reid, J. M. Livingston, M. M. Meier, O. Dubovik, and S.-C. Tsay, J. Geophys. Res. **108**, 8593, doi:10.1029/2002JD002485 (2003).
[29]K. Okada, J. Heintzenberg, K. Kai, and Y. Qin, Geophys. Res. Lett. **28**, 3123–3126, doi:10.1029/2000GL012798 (2001).
[30]P. H. Nadeau, Clay Miner. **20**, 499–514 (1985).
[31]P. Chylek, G. W. Grams, and R. G. Pinninck, Science **193**, 480–482 (1976).
[32]B. Sachweh, H. Umhauer, F. Ebert, H. Buttner, and R. Friehmelt, J. Aerosol Sci. **29**, 1075–1086 (1998).
[33]E. Terrell, D. Beal, and J. Gromala, *Understanding Liquid Particle Counters* (PMS Inc. Boulder, Colorado, 2006).
[34]U. Ruth, "Concentration and size distribution of microparticles in the NGRIP ice core (Central Greenland) during the Last Glacial Period," Ph.D. thesis (Bremen University, 2002).
[35]W. C. Hinds, *Aerosol Technology: Properties, Behavior, and measurement of Airborne Particles*, 2nd ed. (John Wiley and Sons, New York, 1999).
[36]V. Gélinas and D. Vidal, Powder Technol. **203**, 254–264 (2010).
[37]A. Kahn, Clays Clay Miner. **6**(1), 220–236 (1959).
[38]A. P. Tinke, A. Carnicer, R. Govoreanu, G. Scheltjens, L. Lauwerysen, N. Mertens, K. Vanhoutte, and M. E. Brewster, Powder Technol. **186**, 154–167 (2008).
[39]K. T. Whitby and R. A. Vomela, Environ. Sci. Technol. **10**, 801–814 (1967).
[40]J. Gebhart, Part. Part. Syst. Charact. **8**, 40–47 (1991).
[41]M. I. Mishchenko, J. W. Hovenier, and L. D. Travis, *Light Scattering by Nonspherical Particles: Theory, Measurements, and Applications* (Academic Press, San Diego, 1999).
[42]Y. Liu and P. H. Daum, J. Aerosol Sci. **31**, 945–957 (2000).
[43]F. Borghese, P. Denti, and R. Saija, *Scattering from Model Nonspherical Particles* (Springer-Verlag, Berlin-Heidelberg, 2003).
[44]O. Dubovik, J. Geophys. Res. **111**, D11, doi:10.1029/2005JD006619 (2006).
[45]M. A. C. Potenza and P. Milani, J. Nanopart. Res. **16**, 2680 (2014).
[46]M. A. C. Potenza, T. Sanvito, and A. Pullia, AIP Adv. **5**, 117222 (2015).
[47]M. A. C. Potenza, T. Sanvito, and A. Pullia, J. Nanopart. Res. **17**, 110 (2015).
[48]M. A. C. Potenza, T. Sanvito, and G. Fazio, "Optical Characterization of particles for industries," KONA **33**, 310 (2016).
[49]M. A. C. Potenza, T. Sanvito, S. Argentiere, C. Cella, B. Paroli, C. Lenardi, and P. Milani, Sci. Rep. **5**, 18228 (2015).
[50]D. Gabor, Nature **161**, 777 (1948).
[51]W. Goodman, *Introduction to Fourier Optics*, 3rd ed. (Roberts and Company, 2005).
[52]M. A. C. Potenza, K. P. V. Sabareesh, M. Carpineti, M. D. Alaimo, and M. Giglio, Phys. Rev. Lett. **105**, 193901 (2010).
[53]H. C. Van de Hulst, *Light Scattering by Small Particles* (Dover Publications, New York, 1957).
[54]C. F. Bohren and D. R. Huffmann, *Absorption and Scattering by Small Particles* (Wiley, New York, 1983).
[55]M. Dapiaggi, M. Sala, G. Artioli, and M. J. Fransen, Z. Kristallogr. Suppl. **26**, 73–78 (2007).
[56]D. Z. Gunes, R. Scirocco, J. Mewis, and J. Vermant, J. Non-Newton. Fluid **155**, 39–50 (2008).
[57]L. D. Landau and E. M. Lifshitz, *Fluid Mechanics*, 2nd ed. (Pergamon Press, Oxford, 1989).
[58]P. Latimer, A. Brunsting, B. E. Pyle, and C. Moore, Appl. Opt. **17**, 3152–3158 (1978).
[59]M. Mishchenko, L. Travis, R. Kahn, and R. West, J. Geophys. Res. **102**, 16831–16847, doi:10.1029/96JD02110 (1997).
[60]P. Yang *et al.*, J. Aerosol Sci. **38**, 995–1014 (2007).
[61]O. V. Kalashnikova and I. N. Sokolik, Geophys. Res. Lett. **29**, 38-1–38-4, doi:10.1029/2002GL014947 (2002).
[62]O. V. Kalashnikova and I. N. Sokolik, J. Quant. Spectrosc. Radiat. Transfer **87**, 137–166 (2004).
[63]E. M. Purcell and C. R. Pennypacker, Astrophys. J. **186**, 705–714 (1973).
[64]B. T. Draine, Astrophys. J. **333**, 848–872 (1988).
[65]M. A. Yurkin, V. P. Maltsev, and A. G. Hoekstra, J. Quant. Spectrosc. Radiat. Transfer **106**, 546 (2007).
[66]M. A. Yurkin and A. G. Hoekstra, J. Quant. Spectrosc. Radiat. Transfer **106**, 558–589 (2007).
[67]M. A. Yurkin and A. G. Hoekstra, J. Quant. Spectrosc. Radiat. Transfer **112**, 2234–2247 (2011).
[68]A. G. Hoekstra, M. D. Grimminck, and P. M. A. Sloot, Int. J. Mod. Phys. C **9**, 87–102 (1998).
[69]A. G. Hoekstra, M. Frijlink, L. B. F. M. Waters, and P. M. A. Sloot, J. Opt. Soc. Am. **18**, 1944–1953 (2001).
[70]B. R. Jennings and K. Parslo, Proc. R. Soc. London, Ser. A **419**, 137–149 (1988).
[71]J. A. Gallego-Urrea, J. Hammes, G. Cornelis, and M. Hassellöv, J. Nanopart. Res. **16**, 2383 (2014).
[72]R. Jeanicke, J. Aerosol Sci. **3**, 95–111 (1972).
[73]E. G. M. Pelssers, M. A. Cohen, and G. J. Fleer, J. Colloid Interface Sci. **137**, 350–361 (1990).
[74]M. Heim, B. J. Mullins, H. Umhauer, and G. Kasper, Aerosol Sci. **39**, 1019–1031 (2008).
[75]A. Meunier, *Clays* (Springer, Poitiers, 2005).
[76]P. C. Hiemenz and M. Dekker, *Principles of Colloid and Surface Chemistry* (Better World Books, Mishawaka, IN, USA, 1977).
[77]S. C. Glotzer and M. J. Solomon, Nat. Mater. **6**, 557–562 (2007).
[78]V. D. Nguyen, Z. Hu, and P. Schall, Phys. Rev. E **84**, 011607 (2011).
[79]P. B. Shelke, V. D. Nguyen, A. V. Limaye, and P. Schall, Adv. Mater. **25**(10), 1499–1503 (2013).
[80]A. Karnis, H. L. Goldsmith, and S. G. Mason, Can. J. Chem. Eng. **44**, 181–193 (1966).
[81]F. Gauthier, H. L. Goldsmith, and S. G. Mason, Kolloid-Z. Z. Polym. **248**, 1000–1015 (1971).
[82]M. A. C. Potenza, B. Delmonte, S. Villa, T. Sanvito, A. Pullia, and V. Maggi, "Shape and size constraints on dust properties from the old Dome C ice Core, Antarctica," Nat. Sci Rep. (submitted).